Frontiers of Information Technology & Electronic Engineering
www.jzus.zju.edu.cn; engineering.cae.cn; www.springerlink.com
ISSN 2095-9184 (print); ISSN 2095-9230 (online)
E-mail: jzus@zju.edu.cn

Electromagnetic wave property inspired radio environment knowledge construction and artificial intelligence based verification for 6G digital twin channel*

Jialin WANG[†1], Jianhua ZHANG[†‡1], Yutong SUN[1], Yuxiang ZHANG[1], Tao JIANG[2], Liang XIA[2]

[1]*State Key Laboratory of Networking and Switching Technology, Beijing University of Posts and Telecommunications, Beijing 100876, China*

[2]*China Mobile Research Institute, Beijing 100053, China*

[†]E-mail: wangjialinbupt@bupt.edu.cn; jhzhang@bupt.edu.cn

Received May 31, 2024; Revision accepted Oct. 4, 2024; Crosschecked Nov. 20, 2024; Published online Dec. 28, 2024

Abstract: As the underlying foundation of a digital twin network (DTN), digital twin channel (DTC) can accurately depict the electromagnetic wave propagation in the air interface to support the DTN-based 6G wireless network. Since electromagnetic wave propagation is affected by the environment, constructing the relationship between the environment and radio wave propagation is the key to implementing DTC. In the existing methods, the environmental information inputted into the neural network has many dimensions, and the correlation between the environment and the channel is unclear, resulting in a highly complex relationship construction process. To solve this issue, we propose a unified construction method of radio environment knowledge (REK) inspired by the electromagnetic wave property to quantify the propagation contribution based on easily obtainable location information. An effective scatterer determination scheme based on random geometry is proposed which reduces redundancy by 90%, 87%, and 81% in scenarios with complete openness, impending blockage, and complete blockage, respectively. We also conduct a path loss prediction task based on a lightweight convolutional neural network (CNN) employing a simple two-layer convolutional structure to validate REK's effectiveness. The results show that only 4 ms of testing time is needed with a prediction error of 0.3, effectively reducing the network complexity.

Key words: Digital twin channel; Radio environment knowledge (REK) pool; Wireless channel; Environmental information; Interpretable REK construction; Artificial intelligence based knowledge verification

https://doi.org/10.1631/FITEE.2400464 **CLC number:** TN929.5

1 Introduction

With the ever-increasing demand for wireless communication, the sixth generation (6G) wireless network will be more complex (Giordani et al., 2020; Rajoria and Mishra, 2022; Zhang P et al., 2022). Meanwhile, it needs to meet the needs of large-scale users, expand new services, applications, and scenarios, and add new techniques such as cloud-native and information technology virtualization (Chowdhury et al., 2020; Liu GY et al., 2020, 2023; Saad et al., 2020; Zhang P et al., 2020; Ji et al., 2022). The digital twin network (DTN) provides up-to-date network status, closed-loop decision-making, and real-time interaction between the digital and physical worlds by creating a real-time digital replica of physical entities, which adapts the complex 6G wireless network

‡ Corresponding author

* Project supported by the National Key R&D Program of China (No. 2023YFB2904803), the National Natural Science Foundation of China (Nos. 62341128, 62201087, and 62101069), the National Science Fund for Distinguished Young Scholars, China (No. 61925102), the Beijing Natural Science Foundation, China (No. L243002), and the Beijing University of Posts and Telecommunications - China Mobile Research Institute Joint Innovation Center

ORCID: Jialin WANG, https://orcid.org/0000-0001-5985-9061; Jianhua ZHANG, https://orcid.org/0000-0003-0484-6188

(Wu YW et al., 2021; Khan et al., 2022a, 2022b; Masaracchia et al., 2022; Lin et al., 2023). To realize the DTN, it is essential to acquire the accurate wireless channel states between transmitters (TXs) and receivers (RXs), including propagation parameters, fading conditions, and other information related to channels. Therefore, the concept of digital twin channel (DTC) was proposed which enables the online mapping of channel states and variation in the physical world into the digital worlds, emphasizing realized interaction between the channel and the system under the environmental changes (Wang J et al., 2023; Wang H et al., 2024). As the underlying foundation of DTN, DTC enhances the accuracy of real-time channel representation and supports more reliable communication transmission and network optimization for DTN-based 6G wireless networks.

The overall objectives and framework of 6G proposed by the International Telecommunication Union (ITU) identify six major scenarios, with integrated sensing and communication and integrated artificial intelligence (AI) and communication being two among them (ITU, 2022, 2023). The foreseeable development of sensing and AI techniques strongly supports the implementation of DTC (Zhang P et al., 2021; Liu F et al., 2022; Wang ZY et al., 2022). The implementation framework is shown in Fig. 1. First, environmental information and channel data are captured from the physical world for environmental sensing and reconstruction, which involves channel measurement (Rappaport et al., 2019; Zhang JH et al., 2020, 2023), environment-channel dataset construction (Cheng et al., 2023; Shen et al., 2023), and environmental reconstruction (Cui et al., 2019; Poullis, 2020). Then, channel prediction and communication decisions are made in the digital world by constructing the relationship between the environment and the channel, which involves channel large/small-scale parameter prediction (Sun et al., 2022a; Hayashi and Ichige, 2023), low-overhead channel state information (CSI) prediction (Hou et al., 2021; Zhang Z et al., 2024), and decision of beam selection and power allocation (Han et al., 2023; Nguyen et al., 2023; Wu D et al., 2024). Finally, the decision result is fed back from the digital world to the physical world, and the real-time propagation environmental information in the physical world is combined to realize the interaction.

Constructing the relationship between the environment and the channel is important to the six parts because this part is the key to achieving scene generalization and accurate channel presentation in dynamically changing propagation environments. Some studies focused on introducing environmental information into channel representation based on the traditional theory, such as cluster-nuclei-based channel modeling (Zhang JH, 2016), channel twin platform based on global environmental sensing (Miao et al., 2023), channel parameter optimization based on building height (Bor-Yaliniz et al., 2018), and path loss modeling based on point cloud environmental data (Järveläinen et al., 2016). Recently, some studies on obtaining feature matrices representing the relationship between the environment and the channel are directly based on AI. For example, a graph neural network was

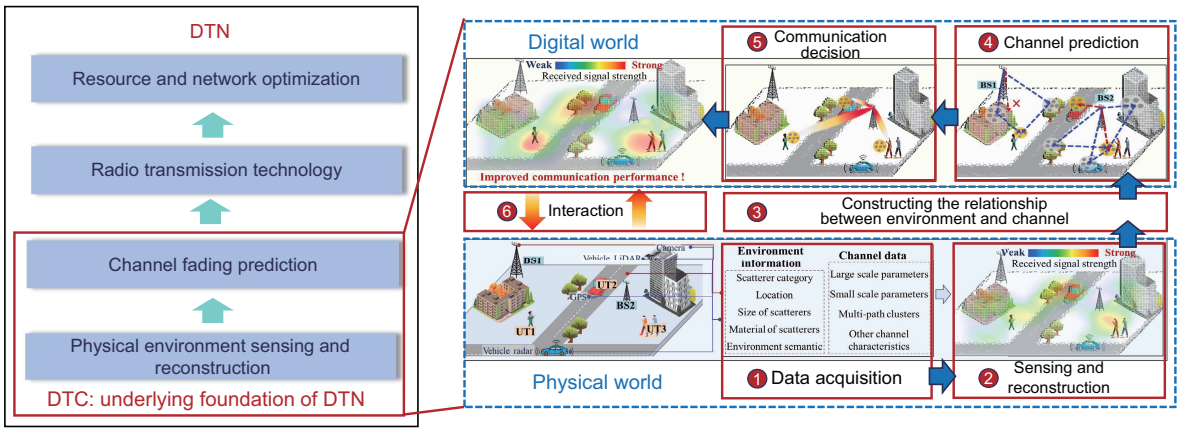

Fig. 1 Implementation framework of the digital twin channel (DTC) which includes six parts (DTN: digital twin network)

used to obtain the relationship between the relative location of TX, RX, and scatterers with regard to channel large/small-scale parameters (Sun et al., 2022b). The relationship between the environment images of different terminal locations and the corresponding channels was constructed for different terminal locations and their corresponding channels through deep learning (Yang WM et al., 2019). A semantic-information-aided communication prediction method was proposed which uses environmental semantics from image data to enhance transmission reliability and reduce latency for beam and blockage state prediction (Yang YW et al., 2023). The environmental semantic features were used to enhance resource allocation in multi-user systems, improving performance and bandwidth efficiency (Zhang P et al., 2023). The relationship between the location and the angle of arrival and the phase variation of the channel was constructed based on deep convolutional neural networks (CNNs), enhancing environmental sensing to achieve efficient indoor localization (Wang XY et al., 2020). A path loss estimation method was proposed which closely resembles simulation values, focusing on the task of path loss prediction using location data (Levie et al., 2021). The current state of research on map construction based on the environment and channel characteristics was reviewed, emphasizing the role of channel knowledge map in enhancing environment-aware wireless communications (Zeng and Xu, 2021; Zeng et al., 2024). However, no research supports that environmental information in one scene affects the electromagnetic wave propagation process or describes how to quantify the influence trends and degree. This is one of the ways to characterize the essential relationship between the environment and the channel, which can be realized by constructing a radio environment knowledge pool (REKP) that we mentioned recently (Wang H et al., 2024). The essential relationship provides the basis for relationship construction and removes environmental information redundancy, which is conducive to simplifying the neural network structure and establishing relationships quickly to support DTC.

As we all know, electromagnetic wave propagation is influenced by the environment. Electromagnetic waves interact with buildings, trees, vehicles, and other environments through reflection and diffraction, and the propagation path forms a geometric relationship between the TX and the RX in the scene. Inspired by this, this study fills in the gap in the interpretable mathematical representation of the relationship between the effective environmental information and the electromagnetic wave propagation process. The main contributions are as follows:

1. A radio environment knowledge (REK) construction method is proposed which quantifies the contributions of reflection, diffraction, and blockage based on easily obtainable three-dimensional (3D) coordinates or online updated location information across various scenarios with different levels of blockage.

2. An effective scatterer determination scheme based on random geometry is proposed which significantly reduces environment redundancy. This scheme achieves $\geq 90\%$ accuracy in selecting effective scatterers and reduces redundancy by 90%, 87%, and 81% in scenarios with complete openness, impending blockage, and complete blockage, respectively.

3. A lightweight path loss prediction method is proposed which uses a simple structured CNN to quickly predict channel parameters. By using the REK spectrum as the input, it effectively reduces the dimensionality of the input data while accurately elucidating deep relationships. The results show that the path loss prediction error is 0.3 with only 5 s of training and 4 ms of testing.

2 Problem formulation

2.1 Scene and assumptions

We consider a sensing-assisted communication single-cell scene. One single base station (BS) serves R user terminals (UTs), employing some sensing devices. The BS acquires the following information: (1) environmental data of stationary objects (such as buildings and trees) provided in the form of images or values, including their locations, materials, and sizes; (2) location information of fast-moving objects acting as reflective entities that do not communicate with the BS; (3) location and channel information of UTs communicating with the BS. Various propagation states exist between the BS and terminals, including line-of-sight (LoS), reflection, scattering, and blockage.

In communication systems, the object that causes the signal to be scattered, attenuated, or reflected is called a scatterer. Scatterers have random

shapes, especially buildings in outdoor urban areas and indoor office areas, which are densely distributed and display various shapes. Given the correlation between signal propagation and scatterers and the interrelationship between channel quality and scatterer information such as shape and location, the following assumptions are made:

The scatterers are modeled as the line Boolean model (Bai et al., 2014). Scatterers are abstracted into different sizes of cuboids, represented by the length of the diagonal segments. The central locations of all line segments are modeled by $\Phi_{\mathrm{s}} = \{\boldsymbol{P}_i | \boldsymbol{P}_i \in \mathbb{R}^2\}$, where $\boldsymbol{P}_i$ represents the location of the center point of the i^{th} scatterer, and the length of each line segment is denoted as $L_i = d(\boldsymbol{P}_{\min}, \boldsymbol{P}_{\max})$, following a uniform distribution $L_i \sim U[L_{\min}, L_{\max}]$ with a mean value of $\mathbb{E}[L]$. $d(\cdot)$ represents the calculation of the Euclidean distance, $\boldsymbol{P}_{\max}$ and $\boldsymbol{P}_{\min}$ the maximum and minimum coordinates within a scatterer, respectively, obtained through sensing devices, and $L_{\min}$ and $L_{\max}$ the minimum and maximum lengths of all line segments, respectively. UTs are considered stationary within short time intervals, with their locations characterized by $\Phi_{\mathrm{u}} = \{\boldsymbol{P}_r | \boldsymbol{P}_r \in \mathbb{R}^2\}$, where $\boldsymbol{P}_r$ and Φ_{u} represent the location coordinates of the r^{th} user and the set comprising all user location coordinates, respectively.

It is assumed that the data transmission links between BS and users currently employ existing beamforming techniques, effectively mitigating interference among multiple users within the same cell. In other words, interference terms can be disregarded in a single-cell millimeter-wave wireless communication system.

2.2 REK pool

To implement DTC, we recently proposed the REK pool (REKP) to focus on how to extract essential relationships from the environment and channel data, emphasizing an online process with feedback and updating capabilities to establish interpretable mapping principles between the two processes (Wang J et al., 2023), as shown in Fig. 2. The core function of REKP is to abstract the channel propagation process from the environment and the channel, thereby facilitating effective compression and intelligent understanding of the underlying mapping rules of the channel. Channel information considered in REKP includes channel parameters, channel state information (CSI), channel propagation, communication tasks affected by channel characteristics, and other information related to wireless channels. The environmental information emphasizes using multimodal, multi-type, and a large amount of environmental data to describe one communication scene comprehensively. Unlike previous studies emphasizing feature mapping obtained through AI algorithms, REKP focuses on generating solidified knowledge through reasoning mechanisms, such as theoretical derivation or semantic construction, thereby improving the interpretability of the channel–environment relationship.

REKP can be viewed as a collection of interpretable relationship mappings $K(\cdot)$ from environmental information $\boldsymbol{\Phi} \in \mathbb{R}^D$ to channel knowledge vectors $\boldsymbol{k} \in \mathbb{C}^J$, expressed as follows:

$$\mathcal{K} = \left\{ K(\cdot) \left| \mathbb{R}^D \to \mathbb{C}^J \right. \right\}, \tag{1}$$

where $\boldsymbol{\Phi}$ represents a collection of D-dimensional

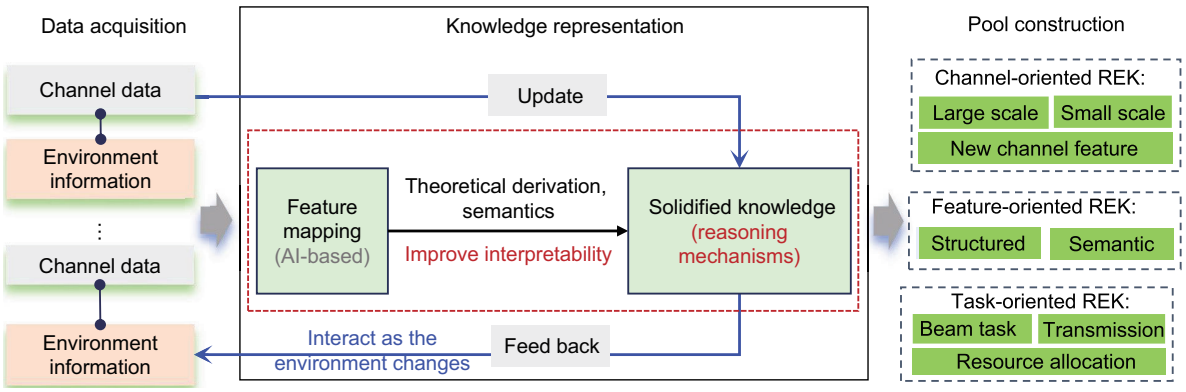

Fig. 2 REKP architecture with its core function being the construction of REK (REK: radio environment knowledge; REKP: REK pool)

environmental information obtained in a physical world. $\mathbb{R}$ includes environmental data about BS, UTs, and scatterers, such as their locations, volumes, materials, and antenna height. D is scenario-specific, varying with different types of scenarios. For example, blockage obstructed in the non-line-of-sight (NLoS) condition is considered, resulting in a larger dimensionality of environmental information in NLoS situations compared with the LoS condition. $\boldsymbol{k} \in \mathbb{C}^J$ denotes the REK that can adapt to environmental changes, where J depends on the channel requirements of communication systems, such as channel-oriented REK, feature-oriented REK, and communication-task-oriented REK. $\mathcal{K}(\cdot)$ represents the process of the REK expression, which constructs the interpretable relationships between the environment and the channel. After quantifying the interpretable relationship through a large amount of environmental information, it exhibits scene generalization without considering the specific characteristics of the communication scene.

3 REK construction

Due to the limitation of antenna height and the influence of surroundings, built-up urban areas rely more heavily on the environment around the antennas. Antennas at the BS are usually installed at rooftop heights. As affected by diffracted signals around building corners, antenna height restrictions, and blockages caused by building layout, the propagation process from BS to UTs can be viewed as the signal originating from the TX, passing through building tops, facades, or edges, nearby buildings, and reaching UTs. This process involves the following three modes of electromagnetic wave propagation, as illustrated in Fig. 3: (1) direct electromagnetic wave to the UTs, where the user is within the LoS range for free space propagation; (2) reflection electromagnetic wave from building walls and ground to UTs; (3) diffraction electromagnetic wave from the sides of the building and the roof of the building near UTs.

The wireless channel is generated through various physical propagation types such as direct radiation, reflection, and diffraction of electromagnetic waves. The channel model can be represented as follows:

$$h(t) = h_{\text{los}}(t) + h_{\text{ref}}(t) + h_{\text{df}}(t), \tag{2}$$

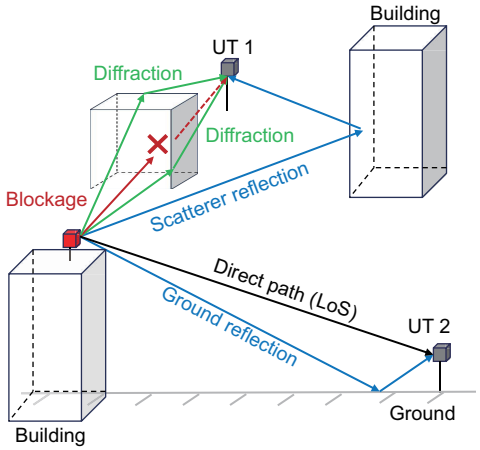

Fig. 3 Electromagnetic wave propagation process from BS to UT, including three types: direct, reflection, and diffraction (BS: base station; UT: user terminal)

$$h_i(t) = \sum_{n=1}^{N_i} \beta_{n,i}(t) \mathrm{e}^{\mathrm{j}(2\pi v_{i,n} t + \phi_{i,n}(t))}, \tag{3}$$

where i is the propagation type, that is, direct radiation, reflection, or diffraction. N_i is the number of channel multipaths generated by type i. $\beta_{n,i}(t)$, $\phi_{i,n}(t)$, and $v_{i,n}$ represent time-varying path loss, phase, and Doppler shift, respectively. Then, REK is constructed from environmental information, delving into the essence of the relationship between the environment and electromagnetic wave propagation.

3.1 Overall construction flow

The values of path gain are determined by the superposition of multiple subpaths, which are generated based on the environmental structure between the TX and the RX. Therefore, the constructed REK k_{ppg} consists of the following components: a representation of propagation contribution based on location information M and knowledge coefficients C, expressed as follows:

$$\boldsymbol{K}(M, C) : \{\boldsymbol{P}_i, \boldsymbol{P}_r, \boldsymbol{P}_t\} \rightarrow k_{\text{ppg}}, \tag{4}$$

where $\boldsymbol{P}_i$, $\boldsymbol{P}_r$, and $\boldsymbol{P}_t$ are the positions of the i^{th} scatterer, the r^{th} RX, and the t^{th} TX, respectively. The propagation contribution explains the contribution levels of propagation modes in the current scene based on the location information, and the knowledge coefficients reflect the weights of propagation modes in different scenes. The flow diagram for the REK construction is shown in Fig. 4.

Step 1: Using environmental information, the

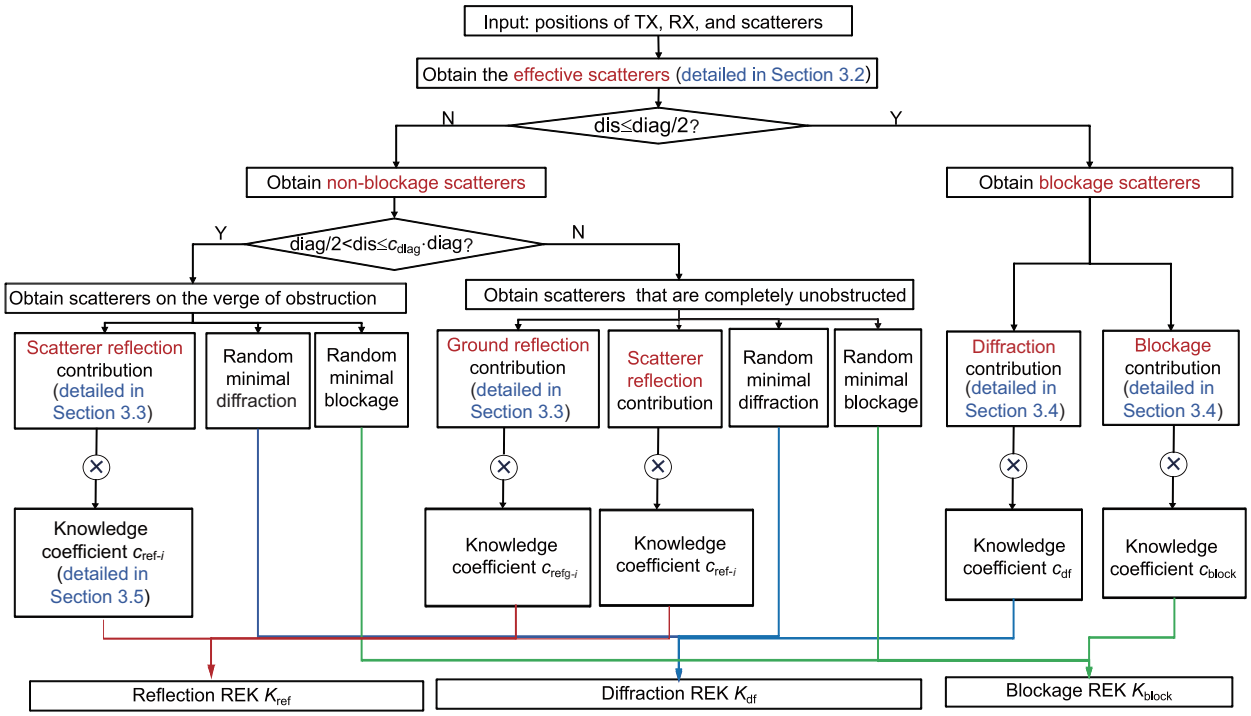

Fig. 4 Flow diagram of the REK construction for one UT (REK: radio environment knowledge; UT: user terminal)

ellipsoid model is constructed based on the stochastic geometry, and the range of effective scatterers involved in electromagnetic wave propagation is determined.

Step 2: Under the current user location, the blockage scatterers that affect LoS propagation are determined, and the corresponding number is saved. If there is a scatterer S, where the distance from its center O to $d_{t,r}$ is less than half of the scatterer's diagonal length, then this scatterer S is classified as a blockage scatterer, denoted as follows:

$$B=\left\{\boldsymbol{P}_i\left|\frac{\boldsymbol{P}_i\cdot(\boldsymbol{P}_t-\boldsymbol{P}_r)}{||\boldsymbol{P}_t-\boldsymbol{P}_r||}<\frac{L_i}{2},\boldsymbol{P}_i\in S\right.\right\},\tag{5}$$

where L_i is the size of the i^{th} scatterer. Those that are not judged as blockage scatterers are classified as non-blockage scatterers.

Step 3: Under the current user location, the scatterers that will become blockage scatterers in the range of non-blockage scatterers are determined and the corresponding numbers are saved. The others are divided into complete openness situations that do not affect LoS.

Step 4: For scatterers on the verge of obstruction, their reflective contribution is computed based on the light reflection theorem in geometric optics (GO) theory (Katz, 2002), acquiring a knowledge coefficient c. In the situation of approaching occlusion, diffraction and blockage contributions are minimal. In this study, their contributions are given random values between 0 and 1. Repeat step 4 until all the propagation knowledge that will become the blockage scatterers is obtained.

Step 5: In the LoS propagation mode, the superlocation of ground reflection and direct waves at the receiving antenna leads to multipath effects. Hence, the contribution of ground reflection cannot be overlooked in LoS scenarios. For scatterers entirely exempt from becoming occlusions, the ground reflection contribution is quantified based on the dual-line reflection model of GO.

Step 6: For blockage scatterers, diffraction propagation losses are quantified based on the uniform geometrical theory of diffraction (UTD) (Pathak and Kim, 2011) and the Fresnel principles (Saunders and Aragón-Zavala, 2007). The blockage contribution in the propagation process is quantified based on geometric relationships.

Step 7: Finally, the contributions of reflection, diffraction, and blockage obtained in the three

situations are consolidated to form the REK toward wireless propagation change and visualized in the form of knowledge spectrum.

3.2 Effective and blockage scatterers

Although the surrounding environment appears static, the environment structure constructed between the TX, scatterers, and RX changes dynamically as the user moves. We divide scatterers in the communication scenario into effective, blockage, and other scatterers, as shown in Fig. 5. Effective scatterers refer to the scatterers that the wireless signal passes through in the transmission process from BS to UT in the propagation mode of reflection, scattering, and so on. Blockage scatterers block the signal from the TX so that the RX cannot accept the signal. In the REK construction process, the same building is judged as a different class of scatterers in the face of different UTs or as the UT moves, related to the user location and the geometric path among TX, RX, and scatterers.

The scatterer ellipsoidal model based on stochastic geometry is established as shown in Fig. 6. TX and RX locations are focal points, and the half-axis lengths along the three orthogonal axes (usually x-, y-, and z-axis) are denoted as a, b, and c, respectively. The focal distance f is the distance $d_{t,r}$ between the TX and the RX, and $\boldsymbol{O}\left(x_0, y_0, z_0\right)$ are the center point coordinates of the ellipsoid. It is assumed that there are S scatterers in the scene, including N effective, B blockage, and other scatterers.

Assuming $b = c = \frac{1}{2}f$ and $a = \sqrt{2b^2}$, there exists a scatterer S with vertex coordinates from $\boldsymbol{P}_{b1}$ to $\boldsymbol{P}_{b8}$. If all eight vertex coordinates are located within the ellipsoid, or if one of the six surfaces of scatterer S intersects with the ellipsoid, then this scatterer is classified as an effective scatterer, denoted as follows:

$$N = \left\{ \boldsymbol{P}_i \left(x_i, y_i, z_i\right) \middle| \frac{2x_i^2}{d_{t,r}^2} + \frac{4y_i^2}{d_{t,r}^2} + \frac{4z_i^2}{d_{t,r}^2} < 1, \boldsymbol{P}_i \in S \right\}. \tag{6}$$

It is worth mentioning that the calculated effective scatterers include scatterers deploying the TX and the RX. However, in practice, this situation is excluded from the set of effective scatterers.

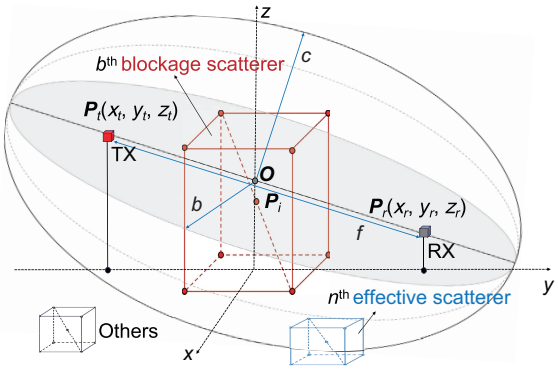

Fig. 6 Scatterer ellipsoidal model based on stochastic geometry

3.3 Reflection contribution

When radio waves pass from one medium to another, a portion reflects, following the law that the angle of reflection equals the angle of incidence. We first propose a reflection point acquisition algorithm based on a random scatterer's shortest path. This algorithm can retrieve reflection points solely through the locations of transmitters, receivers, and scatterers in a random scenario, as illustrated in Algorithm 1.

A face is calculated every four vertices through the center point $\boldsymbol{P}_i$, totaling six faces. The coordinates of the four points of each face are stored as a group, totaling six groups stored in Faces $= \{\boldsymbol{F}_1, \boldsymbol{F}_2, \cdots, \boldsymbol{F}_6\}$. Based on two lines perpendicular to each other on each face, the normal vector of each

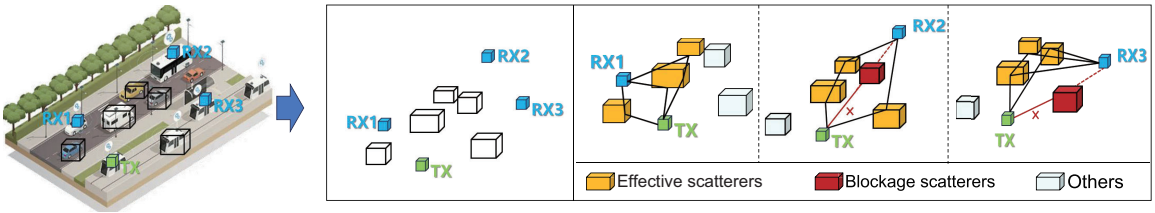

Fig. 5 Effective, blockage, and other scatterers in the communication scenario

Algorithm 1 Reflection point acquisition based on the shortest path of a random scatterer

Faces, Normals $\leftarrow \boldsymbol{P}_i$
loop
  $D_{\min} = \infty$
  for $i \leftarrow 1$ to num(Faces) **do**
    TS $\leftarrow$ Faces $[i]$, $\boldsymbol{P}_t$
    SR $\leftarrow$ Faces $[i]$, $\boldsymbol{P}_r$
    $D_{\text{sum}} = \text{TS} + \text{SR}$
    if $D_{\text{sum}} < D_{\min}$ **then**
      $D_{\min} = \min(D_{\text{sum}})$
      $\mathcal{N} \leftarrow$ Normals $[i]$
      $Q \leftarrow$ Faces $[i]$ [0]
      // Obtain any point on the plane
    end if
    $\hat{\boldsymbol{P}} \leftarrow \boldsymbol{P}_t, \mathcal{N}, Q$
    $\boldsymbol{P}_{\text{R}} \leftarrow \boldsymbol{P}_r, \mathcal{N}, Q, \hat{P}$
  end for
end loop

face is obtained, totaling six normal vectors stored in Normals $= \{\mathbf{Nor}_1, \mathbf{Nor}_2, \cdots, \mathbf{Nor}_6\}$. The sum of the distances from the four vertices on each face to the TX and the RX is expressed as follows:

$$D_{\text{sum}} = \sum_{p=1}^{4} \|\boldsymbol{v}_p - \boldsymbol{P}_t\| + \|\boldsymbol{P}_r - \boldsymbol{v}_p\|, \tag{7}$$

where $\boldsymbol{v}_p \in$ Faces represents the p^{th} vertex on a face, and $\|\cdot\|$ is the norm operation. The face where the smallest D_{sum} is located is the face where the reflection point is located. The specular reflection point of the TX to this surface is expressed as follows:

$$\hat{\boldsymbol{P}} = \boldsymbol{P}_t - \left\langle \boldsymbol{P}_t - \boldsymbol{Q}, \frac{\boldsymbol{\mathcal{N}}}{\|\boldsymbol{\mathcal{N}}\|} \right\rangle \cdot \frac{2\boldsymbol{\mathcal{N}}}{\|\boldsymbol{\mathcal{N}}\|}, \tag{8}$$

where $\boldsymbol{\mathcal{N}}$ is the normal vector of the plane, $\boldsymbol{Q}$ is any point on the plane, and $\langle\cdot\rangle$ is vector dot product operation. In the proposed algorithm, $\boldsymbol{Q}$ is taken as the first vertex in the plane. Then, the reflection point is expressed as follows:

$$\boldsymbol{P}_{\text{R}} = \hat{\boldsymbol{P}} + \frac{\left\langle \boldsymbol{Q} - \hat{\boldsymbol{P}}, \hat{\boldsymbol{N}} \right\rangle \cdot \left(\boldsymbol{P}_r - \hat{\boldsymbol{P}} \right)}{\left\langle \boldsymbol{P}_r - \hat{\boldsymbol{P}}, \hat{\boldsymbol{N}} \right\rangle}, \tag{9}$$

where $\hat{\boldsymbol{N}}$ is normalizing the normal vector $\boldsymbol{\mathcal{N}}$ to a unit vector. Therefore, the reflection contribution from the scatterer and the ground are expressed as follows:

$$K_{\text{ref-}i} = \frac{c_{\text{ref-}i} \|\boldsymbol{P}_t - \boldsymbol{P}_r\|}{\|\boldsymbol{P}_r - \boldsymbol{P}_{\text{R}}\| + \|\boldsymbol{P}_{\text{R}} - \boldsymbol{P}_t\|}, \tag{10}$$

$$K_{\text{refg-}i} = \frac{c_{\text{refg-}i} \|\boldsymbol{P}_t - \boldsymbol{P}_r\|}{\sqrt{(d_t + d_r)^2 + (h_t + h_r)^2}}, \tag{11}$$

where $c_{\text{ref-}i}$ and $c_{\text{refg-}i}$ represent the knowledge coefficients of the i^{th} scatterer and ground reflection, respectively. d_t and d_r are the horizontal distances from the TX and the RX to the ground reflection point, and h_t and h_r are the antenna heights of the TX and the RX, respectively. The geometric relationship among the TX, the RX, the scatterer, and the ground for reflection contribution is shown in Fig. 7.

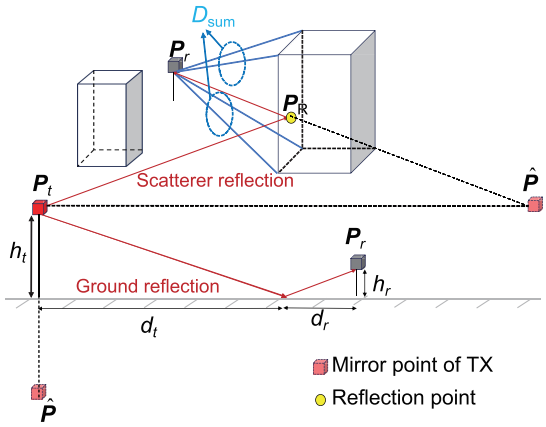

Fig. 7 Geometric relationship for reflection contribution

3.4 Diffraction and blockage contribution

Diffraction refers to the phenomenon where radio waves deviate from their original straight-line propagation path when encountering obstacles during propagation. However, the main signal is not completely blocked and can still be received by users. Along the actual radio wave propagation path, when a building begins to fall within the first Fresnel zone, diffraction losses occur, leading to decreased received power and reduced signal quality. The distance from the vertex of buildings to the line connecting the BS and the UTs is known as the Fresnel clearance. The convention is that the Fresnel clearance is positive when obstructed and negative when unobstructed.

Based on this property, a geometric relationship for diffraction and blockage contributions is designed, as shown in Fig. 8. Using the height of the center of the Fresnel zone as a reference, when the height of the obstruction is h_i, the horizontal distances from the TX and the RX to the obstruction are d_t and d_r, respectively, with the transmitting

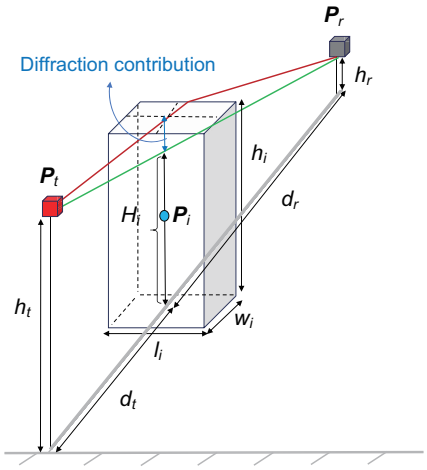

Fig. 8 Geometric relationship for diffraction and blockage contribution

antenna height being h_t and the receiving antenna height being h_r. Then, the height of the center of the Fresnel zone H_i (assuming single scattering) is represented as follows:

$$H_i = h_r + \frac{(h_t - h_r)\, d_r}{d_t + d_r}. \tag{12}$$

The diffraction contribution is the difference between the height of the center of the Fresnel region and the height of the scatterer, expressed as follows:

$$K_{\mathrm{df}} = c_{\mathrm{df}} \left(h_i - H_i\right), \tag{13}$$

where c_{df} is the knowledge coefficient of diffraction.

Furthermore, unlike previous studies, which distinguished the presence of obstruction, the degree of blockage caused by the scatterers during propagation is quantified. The blockage contribution is represented as the ratio of the distance from the blockage scatterer center point to the line connecting the TX and the RX to the length of the line connecting the bottom of the blockage scatterer, multiplied by a knowledge coefficient, expressed as follows:

$$K_{\mathrm{block}} = \frac{\boldsymbol{P}_i \cdot (\boldsymbol{P}_t - \boldsymbol{P}_r)}{||\boldsymbol{P}_t - \boldsymbol{P}_r||} \cdot \frac{c_{\mathrm{block}}}{\sqrt{l_i^2 + w_i^2}}, \tag{14}$$

where l_i and w_i represent the length and width of the i^{th} scatterer, respectively.

3.5 Knowledge coefficient

In scenarios with multiple scatterers between the BS and the UT, the distances from the scatterers to the UT can vary significantly. While location information quantifies the propagation contributions, from an environmental sensing perspective, the distances to the same scatterer for two close RXs are nearly identical. However, the signal loss caused by the scatterer can differ greatly at each RX. Thus, only a few effective scatterers may provide a significant signal gain, and these should be assigned appropriate knowledge coefficients. The knowledge coefficients are $C = \{c_{\mathrm{diag}}, c_{\text{ref-}i}, c_{\text{refg-}i}, c_{\mathrm{df}}, c_{\mathrm{block}}\}$, where c_{diag} denotes the upper bound for impending blockage. When dis $> c_{\mathrm{diag}}$, the communication link from the BS to the UT is in a complete openness scenario. $c_{\text{ref-}i}$, $c_{\text{refg-}i}$, c_{df}, and c_{block} are the knowledge coefficients for scatterer reflection, ground reflection, diffraction, and blockage, respectively.

For the upper bound of impending blockage c_{diag}, a grid search algorithm is employed with a step size of 0.05 within the range of $(1/2, 3/2]$ to identify the most suitable boundary as $c_{\mathrm{diag}} = 0.75$. Coefficients c_{df} and c_{block} are related only to the complete blockage scatterers, both fixed at 1, and do not affect the accuracy of REK spectrum generation. Regarding coefficients $c_{\text{ref-}i}$ and $c_{\text{refg-}i}$, first, based on the visualization of ray tracing (RT) simulation results, some prior knowledge is obtained, and the variation rules of received power, scatterer reflection, and ground reflection are given which are related to the number of different effective scatterers: (1) For reflection points on the same scatterer, the closer the reflection point to the center point of the scatterer, the greater the powers in the reflection path. (2) For reflection points on different scatterers, the smaller the sum of distances from the reflection point to the BS and the UT, the greater the powers in the reflection path. (3) In scenarios of impending blockage and complete blockage, the powers of ground reflection paths are minimal, prioritizing the quantification of scatterer reflection paths. (4) In scenarios of complete openness, the powers of ground reflection paths are significant. However, in the presence of scatterers in the vicinity, scatterers still induce greater losses. (5) The impact of scatterer reflection on received power is greater than that of diffraction and blockage. Based on these findings, we set the threshold range for $c_{\text{ref-}i}$ to $(1, 10]$ and then apply the grid search algorithm with a decrement of one order of magnitude, resulting in $c_{\text{ref-}i} = 5$ and a decrement weight of 0.2. Based on the conclusions drawn from prior knowledge (3) and (4), we find that the effect of ground reflection on received power is minimal,

leading us to set a fixed weight of $c_{\text{refg-}i} = 0.5$.

Ultimately, based on stochastic geometry and electromagnetic propagation theory to acquire propagation knowledge, integrating experience and grid search methods to set knowledge coefficients aims to enhance interpretability between the environment and reflections, diffractions, and blockages.

4 Lightweight CNN construction for REK validation

The constructed REK enhances interpretability, and by using the 3D REK spectrum as the input, we reduce the dimensionality of the input data while accurately elucidating the deep relationship, ensuring prediction accuracy. To validate the constructed REK, we employ a lightweight AI predictor for the path loss prediction task. The simple structure weakens the neural network's feature extraction ability and makes the prediction result more dependent on the knowledge provided by REK.

CNN is a neural network that handles mesh-like topological data structures (Li et al., 2022). The considered input data shape consists of I columns of continuous trajectories, with each column containing J location points and each location point containing the REK matrix, making it suitable as input data for CNNs. This network consists of convolutional, pooling, and fully connected layers. The convolutional and pooling layers form multiple convolutional blocks that extract features from the input. The proposed network structure includes two convolutional layers and a fully connected layer, as shown in Fig. 9.

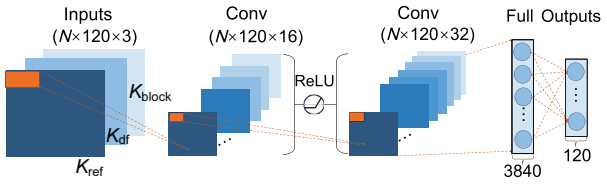

Fig. 9 Lightweight CNN with only two convolutional layers for the path loss prediction task (CNN: convolutional neural network)

The primary function of the convolutional layer is to perceive local features of the input and transform these local features into global representations, expressed as follows:

$$\begin{aligned} S(i,j) &= (\boldsymbol{X} * \boldsymbol{W})(i,j) \\ &= \sum_m \sum_n X(m,n) W(i-m, j-n), \end{aligned} \tag{15}$$

where $\boldsymbol{X}$ is the REK of multiple RX locations, $\boldsymbol{W}$ is the convolutional kernel, and m and n are the indices for the convolution operation. The numbers of input and output data channels are 3 and 16, respectively, with a 3×3 convolution kernel. The second convolutional layer has 512 neurons, with the numbers of input and output data channels being 16 and 32, respectively. Nonlinear transformations of data are conducted using the ReLU activation function between the two convolutional layers. The fully connected layer unfolds the feature maps extracted by convolutional layers into a one-dimensional vector. This vector is then transformed through a matrix multiplication with weight $\boldsymbol{W}$ and an addition of bias b, producing the final output, expressed as $y = f(\boldsymbol{W}\boldsymbol{x} + b)$. The input to the fully connected layer is a 120×3 feature matrix.

5 REK verification

A quantitative evaluation for REK and a performance comparison based on the proposed lightweight CNN predictors are conducted. This section reports some representative numerical results in terms of a knowledge graph of propagation contribution, scatterer selection and prediction accuracy, and training time.

5.1 Datasets and simulation configuration

All datasets are generated from the Beijing University of Posts and Telecommunications and China Mobile Communications Group DataAI-6G Dataset (BUPTCMCC-DataAI-6G Dataset) (Shen et al., 2023), which can be downloaded from https://jiutian.10086.cn/open/#/setList?platform=OpenInnovation. From the 646 m × 290 m simulation scene, to generate channel data from the TX to the RX deployment area, path loss is obtained, and path files are simulated. The size of the RX2 deployment area is 59.5 m × 30.0 m. Starting from the bottom left corner of the RX deployment area, every 61 RXs form a row with a spacing of 0.5 m, totaling 120 rows arranged to the top right corner, totaling 7320 RXs. The specific simulation

configuration is shown in Table 1.

Table 1 Simulation configuration

Parameter	Value/Description
Scenario size	646 m × 290 m
Frequency	3.5 GHz
Bandwidth	200 MHz
TX antenna type	Omnidirectional
TX antenna height	20 m
RX deployment size	59.5 m × 30.0 m
RX antenna type	Omnidirectional
RX antenna height	1.5 m
RX deployment spacing	0.5 m

For REK verification, an outdoor street is considered as the simulation scenario with small changes in the environmental structure of the TX, scatterer, and RX caused by the slow movement of the user. In such a scenario, there is no need to rerun from the beginning. We obtain only the scatterer position coordinates either offline or online to achieve fast and high-precision channel parameter prediction. Environmental information is obtained from the simulation file, including the 3D coordinates of the TX and the RX and each scatterer's maximum and minimum 3D coordinates. The center point coordinates of the scatterers are calculated based on the maximum and minimum 3D coordinates. The simulation scenario's two-dimensional (2D) and 3D perspectives are shown in Fig. 10, providing labels for each scatterer to evaluate the accurate selection of effective scatterers. There are a total of 7320 data samples, each with one propagation knowledge matrix that includes three types of propagation: reflection, diffraction, and blockage. Seventy-five percent of the data are allocated for training, and the remaining 25% for testing, and it is ensured that the training data and the testing data are at different RX locations. Table 2 shows the specific network hyperparameter configuration. All simulation results are uniformly tested on devices with i5-14600kf (32 GB) configurations and Nvidia RTX 4080 (16 GB) and calculated more than 10 times to take the average.

A training process starts from an initial state where all weights and biases are randomly selected. Normalized root mean squared error (NRMSE), a metric for measuring prediction accuracy, is chosen as the cost function in this study for training, expressed as follows:

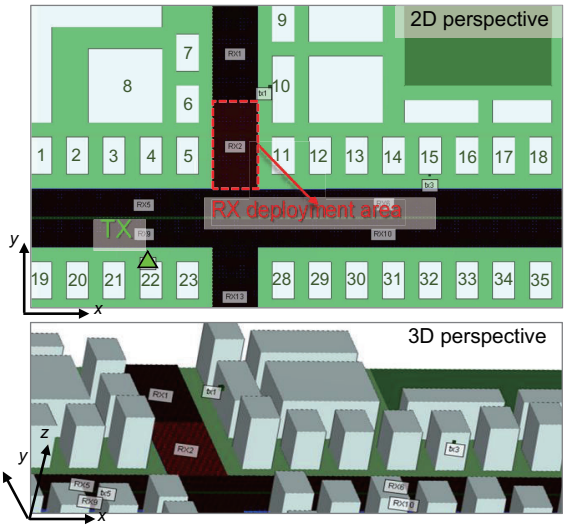

Fig. 10 Two- and three-dimensional perspectives of the simulation scene, scatterer numbers, TX location, and RX deployment area

Table 2 Hyperparameter configuration

Parameter	Value/Description
Batch size	16
Cost function	NRMSE
Actuation function	ReLU
Learning rate	0.001
Number of training data samples	5760
Number of test data samples	1560
Number of hidden neurons	16, 32, 120

NRMSE: normalized root mean squared error

$$\mathrm{NRMSE}=\sqrt{\frac{\sum_{l=1}^{L_{\mathrm{test}}}\left(Y_{\mathrm{real}}(l)-Y_{\mathrm{pred}}(l)\right)^2}{L_{\mathrm{test}}\sigma^2}}, \tag{16}$$

where L_{test} is the sample number of the constructed REK matrices, $Y_{\mathrm{real}}(l)$ and $Y_{\mathrm{pred}}(l)$ are the real and predicted output values at the other location l, respectively, and σ^2 is the variance of $Y_{\mathrm{pred}}(l)$. The training process is iterated until the network completes the specified training epochs or meets the expected convergence condition. Once completed, the trained network can predict path loss at other locations.

5.2 REK generation and evaluation

First, verifying whether the constructed REK can correspond to the effects of reflection, diffraction, and blockage in an actual scene is necessary. The

simulated paths obtained by the RT are close to the actual paths in this study. Fig. 11 shows the scatterers traversed by the first 10 paths arranged in reverse order of power under three scenarios: complete openness, impending blockage, and complete blockage. The color of the paths indicates the received power at the RX, with closer proximity to red indicating higher received power. The RX labels associated with the three scenarios are RX = 40, 73, and 107.

Table 3 presents the accuracy and reduced redundancy of effective scatterer selection based on the ellipsoid model using stochastic geometry. Considering that scatterers closer to the RX have a greater impact, we propose a scatterer selection accuracy evaluation metric with uniformly decreasing weights, expressed as follows:

$$A = \sum_{i \in S_{\text{select}}} w_i, \tag{17}$$

where

$$w_i = \begin{cases} 0.3 - (n-1) \times 0.5, \ i = S_{\text{real}}^{(n)}, \\ 0, \ i \in S_{\text{real}}, i \neq S_{\text{real}}^{(n)}, \\ -0.1, \ i \notin S_{\text{real}}, \end{cases}$$

S_{select} represents the effective scatterer labels selected by the proposed method, S_{real} represents the scatterer labels traversed by the first 25 paths obtained by the RT method, sorted by received power in reverse order, and $S_{\text{real}}^{(n)}$ represents the first n values in S_{real}, $n = 5$. When the proposed method assigns scatterer indices corresponding to one of the first five values in S_{real}, a weighting scheme is applied starting with a weight of 0.3 for the first value, decreasing sequentially by 0.05 for the second to fifth values. Weight of 0 is assigned to scatterers that are in S_{real} but not among $S_{\text{real}}^{(5)}$, while scatterers not belonging to S_{real} are assigned a weight of –0.1. The final selection accuracy is obtained by summing these weights. In the cases of impending blockage and complete blockage, the accuracy of identified scatterers is 90%, with a slight decrease in accuracy for complete openness. In LoS conditions, the majority of the path received power comes from the direct path, where accurately selecting the majority of scatterers providing subpath power does not significantly impact subsequent knowledge construction. As for the reduced redundancy, it can be expressed as $\Re = 1 - \frac{N_{\text{es}}}{N_{\text{ts}}}$, where N_{es} is the

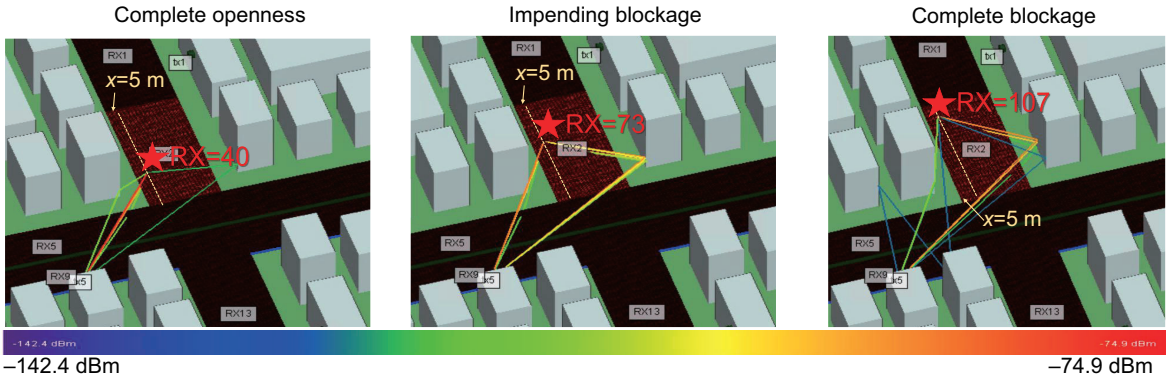

Fig. 11 Scatterers and main path links passing from the TX to the RX under the conditions of complete openness, impending blockage, and complete blockage (number of paths = 10 and x = 5 m, where x is the horizontal distance to the left roadside) (References to color refer to the online version of this figure)

Table 3 Accuracy and redundancy reduction of obtaining scatterers based on geometric construction method

Case	Scatterer number		Accuracy	Reduction in redundant
	Proposed method	RT method*	(%)	data (%)
Complete openness	4, 5, 23	5, 11, 23, 4, 10, 6, 2, 22	65	90
Impending blockage	4, 5, 11, 23	5, 11, 23, 4, 10, 6	90	87
Complete blockage	4, 5, 6, 8, 11, 23	11, 6, 5, 4, 23, 10, 27, 28, 29, 7	90	81

* Sorted by received power in reverse order. RT: ray tracing

number of effective scatterers and N_{ts} is the total number of scatterers. Our proposed effective scatterer determination algorithm greatly reduces input data redundancy, especially in blockage scenarios, achieving a reduction in redundant data of 87% and 81% in impending blockage and complete blockage cases, respectively.

Fig. 12 shows the dual y-axis plot of REK corresponding to the path loss curve locations in the scenarios given in Fig. 11, where the left y-axis is path loss and the right y-axis denotes contributions from reflection, diffraction, and blockage. The x-axis indicates the location labels of the RX. From the whole perspective, when RX $<$ 80, the impact of REK is minimal, whereas for RX $>$ 80, contributions from reflection (RC), diffraction (DC), and blockage (BC) become more intricate. In the region where the RX ranges from 0 to 60, representing a completely open scenario, the path loss is stable with minimal propagation contributions. Most received power originates from the direct path, resulting in low path loss. At RX = 73, a notable increase in reflection contribution is observed with K_{ref} = 8.25, capturing the reflective effects introduced by surrounding scatterers. In complete blockage scenarios with RX $>$ 80, the maximum reflection contribution peaks at 36.07, occurring at RX = 107. The maximum values for diffraction and obstruction contributions are 28.51 and 24.18, respectively, and they exhibit a gradual decrease trend. However, a significant increase is observed compared to complete openness and impending blockage scenarios. Furthermore, in conjunction with Fig. 11, it is evident that at RX = 107, the reflection paths are complex, with the total power from reflection paths significantly exceeding that from diffraction paths. Thus, it confirms that the proposed REK construction method effectively characterizes the contributions of different propagation types to path loss at various locations. The complete REK quantification spectrum along this trajectory is illustrated in Fig. 13, with an enlarged subgraph depicting the portion where RX $>$ 80. In subsequent predictions, the REK spectrum for each trajectory is used as the input.

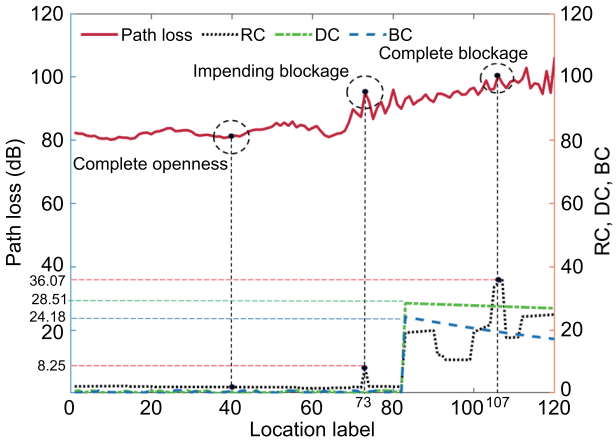

Fig. 12 Path loss curve and the reflection, diffraction, and blockage contributions under the corresponding locations (x = 5 m) (RC: reflection contribution; DC: diffraction contribution; BC: blockage contribution) (References to color refer to the online version of this figure)

5.3 Prediction performance

In this subsection, the prediction performances of path loss prediction methods are compared, including the unprocessed location data based method, the environmental feature based method, and our proposed REK-based method. The unprocessed location data based method uses the location information of TX, RX, and effective scatterers directly for path loss prediction without undergoing any preprocessing. The environmental feature based method constructs environmental features using the processing techniques outlined in Sun et al. (2022a) from location information, incorporating four features representing volume, distance, bias, and blockage to construct a feature matrix for path loss prediction. The proposed REK-based method uses easily obtainable location information to elucidate the deep relationship between the environment and the channel, generating the REK spectrum as the output for path loss prediction. To ensure that the performance gains of different methods originate from different relationship constructions between the environment and the channel, the same neural network and network structure are used, that is, the lightweight CNN with two convolutional layers introduced in Section 4. Hyperparameter optimization is conducted based on the corresponding input data features to guarantee optimal predictive outputs. The predicted values generated by the three methods are compared and evaluated against path loss data from the RT as an approximation of true values.

Table 4 provides a performance comparison of the three methods in terms of the prediction error, training time, and testing time. It is evident that the

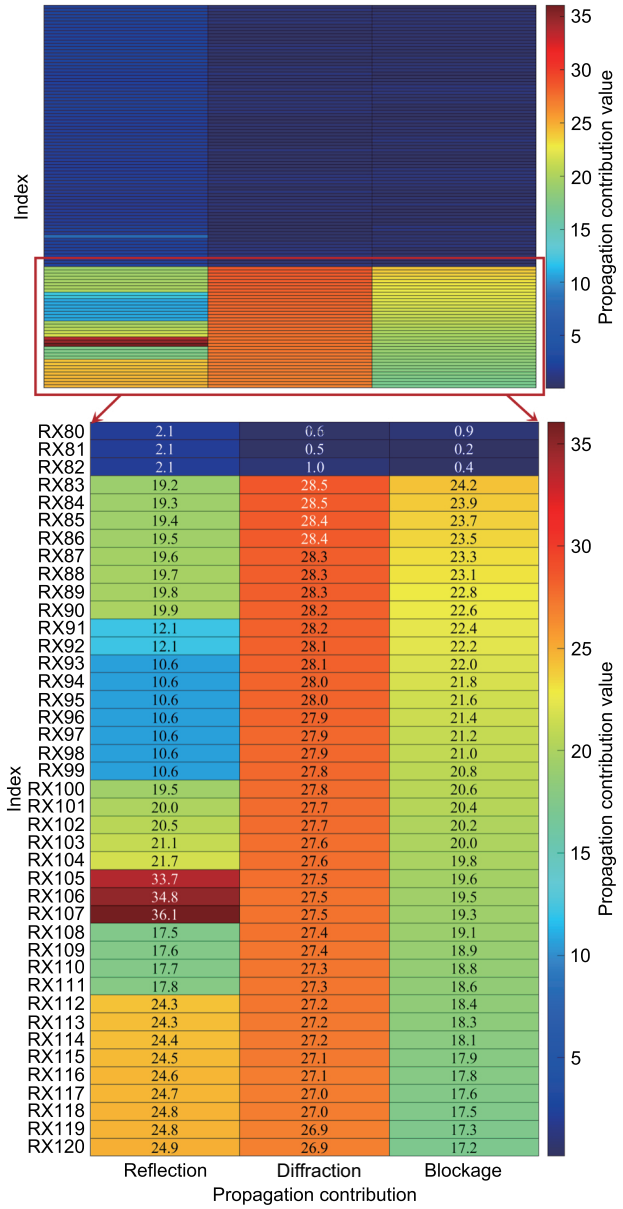

Fig. 13 Radio environment knowledge spectrum for reflection, diffraction, and blockage ($x = 5$ m)

proposed REK-based method demonstrates a clear advantage in prediction accuracy, yielding improvements of 29.4% and 27.5% compared to the direct utilization of location data and the environmental feature based method, respectively. This complexity is primarily reflected in testing time: generating channel parameters using RT takes approximately 20 min, while predictions based on REK require only a few milliseconds, resulting in a reduction in time complexity by five orders of magnitude. This millisecond-level speed guarantees the feasibility of online communication predictions.

Fig. 14 shows the comparison curves of the predicted and true values, obtained by REK-based, unprocessed location data based, and environmental

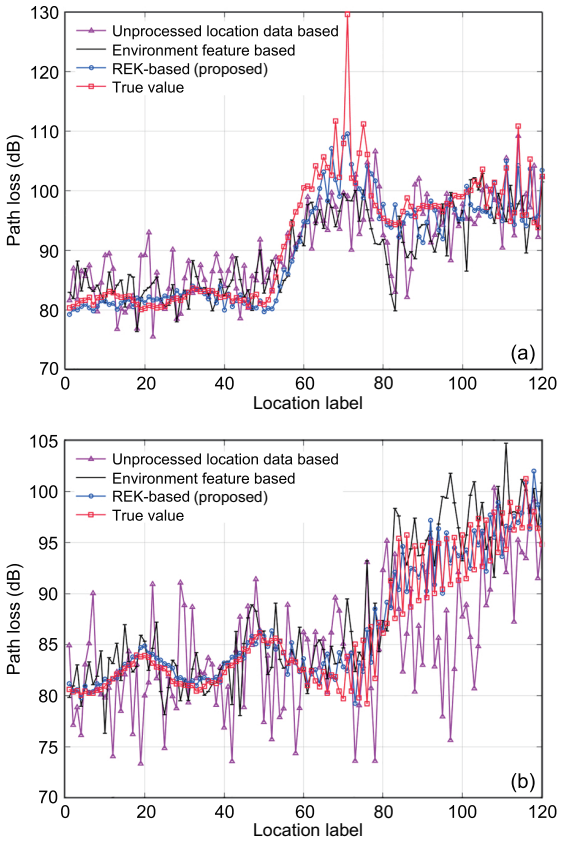

Fig. 14 Path loss prediction results of the proposed REK-based method and the comparative methods: (a) $x = 25$ m; (b) $x = 30$ m (REK: radio environment knowledge)

Table 4 Comparison of path loss prediction performances among the proposed REK-based, unprocessed location data based, and environmental feature based methods

Method	NRMSE	Training time (s)	Testing time (s)
Unprocessed location data based	0.565	8.21	0.227
Environmental feature based	0.456	7.67	0.170
Proposed REK-based	0.271	4.07	0.004

NRMSE: normalized root mean squared error; REK: radio environment knowledge

feature based methods for the horizontal distance at 25 m and 30 m from the left roadside. When $x = 25$ m, the trajectory is located in the middle of the road, and the buildings on both sides affect the radio waves. When $x = 30$ m, the trajectory moves toward the right side of the road, potentially experiencing more complex propagation types influenced by the buildings on the right roadside. As shown in the figure, the proposed REK-based method is better than the existing methods for characterizing the trend of path loss, especially in challenging situations such as complete blockage where the index is larger than 80. Combined with Fig. 11, it is evident that when $x = 30$ m, near the right roadside, the radio experiences a diverse range of propagation types influenced by complex scatterers. It is obvious from Fig. 14b that the prediction results obtained by the unprocessed location data based method under the condition of complete blockage are not in line with reality. Although the environmental feature based method predicts the trend of path loss, the accuracy is still far from that of our proposed REK-based method. Under complete openness scenarios where the index is within 0–60, the predicted fitting curve of the proposed REK-based method almost coincides with the curve of true values.

From the view of statistical analysis, the nonlinear approximations of the proposed REK-based and the comparative methods are further evaluated, including the comparison of cumulative distribution function (CDF) and quantitative statistical values. In Fig. 15, the effectiveness of the proposed REK-based method is validated by comparing the CDF plots of the predicted and true values. Compared with the comparative method, the proposed REK-based method has a more consistent trend with the true values. This means that the constructed REK spectrum is more capable of capturing the complete process of path loss caused by the superposition of different propagation types, especially in the case of complete blockage where there are more times of blocking and reflection, as shown in Fig. 15b. Furthermore, the model does not predict the portion where the path loss is larger than 110 dB, as shown in Fig. 15a. This segment displays sudden spikes in one to two path loss values, collectively identified as outliers in path loss. This phenomenon corresponds to Fig. 14a. Table 5 presents the quantitative statistical data of predicted and true path loss, including the upper and lower quartiles (UQ and LQ), upper and lower bounds (UB and LB), median values (MED), and outliers (OL). It is obvious that the statistical values of the proposed REK-based method are closer to the true values, which verifies the validity of the constructed REK.

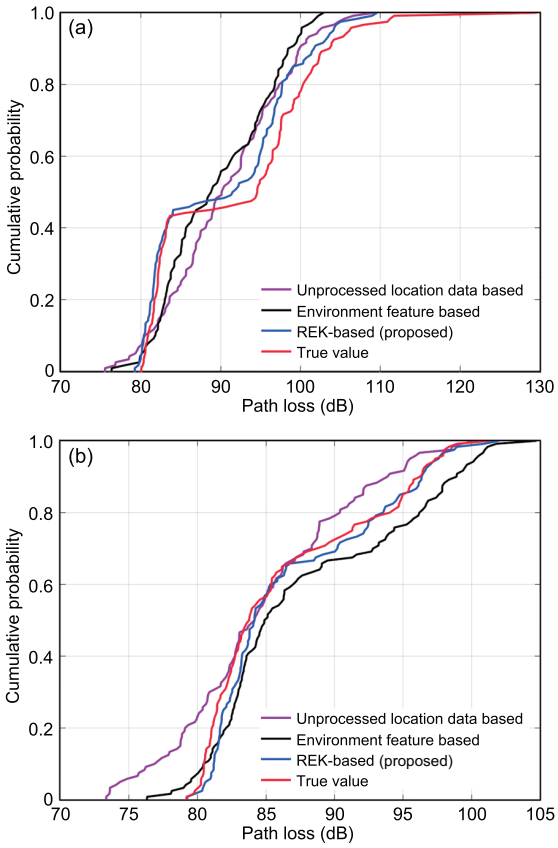

Fig. 15 CDF plots of the proposed REK-based method and the comparative methods: (a) $x = 25$ m; (b) $x = 30$ m (CDF: cumulative distribution function; REK: radio environment knowledge) (References to color refer to the online version of this figure)

6 Conclusions

Constructing the relationship between the environment and the channel is crucial for mapping real-world physical channels to generate DTC in the digital world. In this study, we propose a method of REK construction inspired by electromagnetic wave properties to deal with the high complexity of the construction process caused by the redundancy of environmental information and the ambiguity of relationship correlation. First, an effective scatterer determination scheme based on random geometry is proposed which reduces redundancy by 90%, 87%, and

Table 5 Quantification of the box plot for REK-based and compared methods in path loss prediction tasks

x	Method	UQ	LQ	UB	LB	MED	OL
25 m	Unprocessed location data based	96.2239	85.1638	112.8140	68.5737	90.1895	0
	Environmental feature based	95.6194	83.6279	113.6066	65.6407	88.8534	0
	Proposed REK-based	97.0783	81.6562	120.2114	58.5231	91.7083	0
	True value	99.1884	82.1302	124.7756	56.5430	94.5806	1
30 m	Unprocessed location data based	88.8545	80.3801	101.5660	67.6685	84.1815	0
	Environmental feature based	94.3520	82.6382	111.9226	65.0675	84.9958	0
	Proposed REK-based	92.2948	81.9931	107.7473	66.5406	84.1580	0
	True value	91.3047	81.4328	106.1127	66.6249	83.7807	0

REK: radio environment knowledge; UQ: upper quartile; LQ: lower quartile; UB: upper bound; LB: lower bound; MED: median value; OL: outlier

81% in scenarios with complete openness, impending blockage, and complete blockage, respectively. Subsequently, based on the concept of REKP, the contributions of electromagnetic wave reflection, diffraction, and the blockage of scatterers are quantified using the locations of TX, RX, and scatterers, and REK is visualized in the form of knowledge spectrum. Experiments on a path loss prediction task based on a lightweight CNN are conducted to validate REK's effectiveness. The results show that using REK as an input maintains a prediction error of 0.3 with only two convolutional layers in the network structure, with a testing time of only 4 ms. In future studies, we will focus on knowledge construction for high-speed dynamic scenarios, built on the proposed approach to incorporate an online rapid response mechanism that can adapt to significant changes in the propagation environment occurring over short time intervals. We also plan to investigate methods for constructing radio environment knowledge that considers material properties, incorporating a more diverse range of scatterer wooden trees and metallic vehicles.

Contributors

Jialin WANG, Jianhua ZHANG, Yutong SUN, and Yuxiang ZHANG designed the research. Jialin WANG and Yuxiang ZHANG conducted the investigation. Jialin WANG developed the methodology, performed visualization, validated the results, and drafted the paper. Jialin WANG and Jianhua ZHANG revised and finalized the paper. Tao JIANG and Liang XIA managed project administration and acquired funding.

Conflict of interest

Jianhua ZHANG is an executive associate editor-in-chief of *Frontiers of Information Technology & Electronic Engineering*, and she was not involved with the peer review process of this paper. All the authors declare that they have no conflict of interest.

Data availability

The datasets used can be downloaded from https://jiutian.10086.cn/open/#/setList?platform=OpenInnovation. The other data that support the findings of this study are available from the corresponding author upon reasonable request.

References

Bai TY, Vaze R, Heath RW, 2014. Analysis of blockage effects on urban cellular networks. *IEEE Trans Wirel Commun*, 13(9):5070-5083. https://doi.org/10.1109/TWC.2014.2331971

Bor-Yaliniz I, Szyszkowicz SS, Yanikomeroglu H, 2018. Environment-aware drone-base-station placements in modern metropolitans. *IEEE Wirel Commun Lett*, 7(3):372-375. https://doi.org/10.1109/LWC.2017.2778242

Cheng X, Huang ZW, Bai L, et al., 2023. M^{3}SC: a generic dataset for mixed multi-modal (MMM) sensing and communication integration. *China Commun*, 20(11):13-29. https://doi.org/10.23919/JCC.fa.2023-0268.202311

Chowdhury MZ, Shahjalal M, Ahmed S, et al., 2020. 6G wireless communication systems: applications, requirements, technologies, challenges, and research directions. *IEEE Open J Commun Soc*, 1:957-975. https://doi.org/10.1109/OJCOMS.2020.3010270

Cui Y, Li QQ, Yang BS, et al., 2019. Automatic 3-D reconstruction of indoor environment with mobile laser scanning point clouds. *IEEE J Sel Top Appl Earth Obs Remote Sens*, 12(8):3117-3130. https://doi.org/10.1109/JSTARS.2019.2918937

Giordani M, Polese M, Mezzavilla M, et al., 2020. Toward 6G networks: use cases and technologies. *IEEE Commun Mag*, 58(3):55-61. https://doi.org/10.1109/MCOM.001.1900411

Han DR, Ye Q, Peng HX, et al., 2023. Two-timescale learning-based task offloading for remote IoT in integrated satellite-terrestrial networks. *IEEE Int Things J*, 10(12):10131-10145. https://doi.org/10.1109/JIOT.2023.3237209

Hayashi T, Ichige K, 2023. A deep-learning method for path loss prediction using geospatial information and path profiles. *IEEE Trans Antenn Propag*, 71(9):7523-7537. https://doi.org/10.1109/TAP.2023.3295890

Hou WH, Sun JL, Gui G, et al., 2021. Federated learning for DL-CSI prediction in FDD massive MIMO systems. *IEEE Wirel Commun Lett*, 10(8):1810-1814. https://doi.org/10.1109/LWC.2021.3081695

ITU, 2022. Future Technology Trends of Terrestrial International Mobile Telecommunications Systems Towards 2030 and Beyond. Report ITU-R M.2516-0, ITU, Geneva.

ITU, 2023. Framework and Overall Objectives of the Future Development of IMT for 2030 and Beyond. Recommendation ITU-R M.2160-0, ITU, Geneva.

Järveläinen J, Nguyen SLH, Haneda K, et al., 2016. Evaluation of millimeter-wave line-of-sight probability with point cloud data. *IEEE Wirel Commun Lett*, 5(3):228-231. https://doi.org/10.1109/LWC.2016.2521656

Ji XS, Wu JX, Jin L, et al., 2022. Discussion on a new paradigm of endogenous security towards 6G networks. *Front Inform Technol Electron Eng*, 23(10):1421-1450. https://doi.org/10.1631/FITEE.2200060

Katz M, 2002. Introduction to Geometrical Optics. World Scientific, River Edge, USA. https://doi.org/10.1142/5135

Khan LU, Saad W, Niyato D, et al., 2022a. Digital-twin-enabled 6G: vision, architectural trends, and future directions. *IEEE Commun Mag*, 60(1):74-80. https://doi.org/10.1109/MCOM.001.21143

Khan LU, Han Z, Saad W, et al., 2022b. Digital twin of wireless systems: overview, taxonomy, challenges, and opportunities. *IEEE Commun Surv Tutor*, 24(4):2230-2254. https://doi.org/10.1109/COMST.2022.3198273

Levie R, Yapar Ç, Kutyniok G, et al., 2021. RadioUNet: fast radio map estimation with convolutional neural networks. *IEEE Trans Wirel Commun*, 20(6):4001-4015. https://doi.org/10.1109/TWC.2021.3054977

Li ZW, Liu F, Yang WJ, et al., 2022. A survey of convolutional neural networks: analysis, applications, and prospects. *IEEE Trans Neur Netw Learn Syst*, 33(12):6999-7019. https://doi.org/10.1109/TNNLS.2021.3084827

Lin XQ, Kundu L, Dick C, et al., 2023. 6G digital twin networks: from theory to practice. *IEEE Commun Mag*, 61(11):72-78. https://doi.org/10.1109/MCOM.001.2200830

Liu F, Cui YH, Masouros C, et al., 2022. Integrated sensing and communications: toward dual-functional wireless networks for 6G and beyond. *IEEE J Sel Areas Commun*, 40(6):1728-1767. https://doi.org/10.1109/JSAC.2022.3156632

Liu GY, Huang YH, Li N, et al., 2020. Vision, requirements and network architecture of 6G mobile network beyond 2030. *China Commun*, 17(9):92-104. https://doi.org/10.23919/JCC.2020.09.008

Liu GY, Deng J, Zheng QB, 2023. 6G autonomous mobile network enabled by digital twin network. *ZTE Technol J*, 29(3):2-7 (in Chinese). https://doi.org/10.12142/ZTETJ.202303002

Masaracchia A, Sharma V, Canberk B, et al., 2022. Digital twin for 6G: taxonomy, research challenges, and the road ahead. *IEEE Open J Commun Soc*, 3:2137-2150. https://doi.org/10.1109/OJCOMS.2022.3219015

Miao YH, Zhang YX, Zhang JH, et al., 2023. Demo abstract: predictive radio environment for digital twin communication platform via enhanced sensing. Proc IEEE Conf on Computer Communications Workshops, p.1-2. https://doi.org/10.1109/INFOCOMWKSHPS57453.2023.10225977

Nguyen MT, Song J, Kwon S, et al., 2023. Power allocation for adaptive-connectivity wireless networks under imperfect CSI. *IEEE Trans Commun*, 71(7):4328-4343. https://doi.org/10.1109/TCOMM.2023.3277041

Pathak PH, Kim Y, 2011. A uniform geometrical theory of diffraction (UTD) for curved edges illuminated by electromagnetic beams. Proc 30th URSI General Assembly and Scientific Symp, p.1-4. https://doi.org/10.1109/URSIGASS.2011.6050243

Poullis C, 2020. Large-scale urban reconstruction with tensor clustering and global boundary refinement. *IEEE Trans Patt Anal Mach Intell*, 42(5):1132-1145. https://doi.org/10.1109/TPAMI.2019.2893671

Rajoria S, Mishra K, 2022. A brief survey on 6G communications. *Wirel Netw*, 28(7):2901-2911. https://doi.org/10.1007/s11276-022-03007-8

Rappaport TS, Xing YC, Kanhere O, et al., 2019. Wireless communications and applications above 100 GHz: opportunities and challenges for 6G and beyond. *IEEE Access*, 7:78729-78757. https://doi.org/10.1109/ACCESS.2019.2921522

Saad W, Bennis M, Chen MZ, 2020. A vision of 6G wireless systems: applications, trends, technologies, and open research problems. *IEEE Netw*, 34(3):134-142. https://doi.org/10.1109/mnet.001.1900287

Saunders SR, Aragón-Zavala AA, 2007. Antennas and Propagation for Wireless Communication Systems. John Wiley & Sons, Chichester, UK.

Shen ZB, Yu L, Zhang YX, et al., 2023. DataAI-6G: a system parameters configurable channel dataset for AI-6G research. Proc IEEE Globecom Workshops, p.1910-1915. https://doi.org/10.1109/GCWkshps58843.2023.10464657

Sun YT, Zhang JH, Zhang YX, et al., 2022a. Environment features-based model for path loss prediction. *IEEE Wirel Commun Lett*, 11(9):2010-2014. https://doi.org/10.1109/LWC.2022.3192516

Sun YT, Zhang JH, Zhang YX, et al., 2022b. Environment information-based channel prediction method assisted by graph neural network. *China Commun*, 19(11):1-15. https://doi.org/10.23919/JCC.2022.11.001

Wang H, Zhang JH, Nie GF, et al., 2024. Digital twin channel for 6G: concepts, architectures and potential applications. https://arxiv.org/abs/2403.12467

Wang J, Zhang Y, Zhang J, et al., 2023. Towards 6G digital twin channel using radio environment knowledge pool. https://arxiv.org/abs/2312.10287

Wang XY, Wang XY, Mao SW, 2020. Deep convolutional neural networks for indoor localization with CSI images. *IEEE Trans Netw Sci Eng*, 7(1):316-327. https://doi.org/10.1109/TNSE.2018.2871165

Wang ZY, Sun YH, Yuan S, 2022. Intelligent radio access networks: architectures, key techniques, and experimental platforms. *Front Inform Technol Electron Eng*, 23(1):5-18. https://doi.org/10.1631/FITEE.2100305

Wu D, Zeng Y, Jin S, et al., 2024. Environment-aware hybrid beamforming by leveraging channel knowledge map. *IEEE Trans Wirel Commun*, 23(5):4990-5005. https://doi.org/10.1109/TWC.2023.3323941

Wu YW, Zhang K, Zhang Y, 2021. Digital twin networks: a survey. *IEEE Int Things J*, 8(18):13789-13804. https://doi.org/10.1109/JIOT.2021.3079510

Yang WM, Zhang XC, Tian YP, et al., 2019. Deep learning for single image super-resolution: a brief review. *IEEE Trans Multim*, 21(12):3106-3121. https://doi.org/10.1109/TMM.2019.2919431

Yang YW, Gao FF, Tao XM, et al., 2023. Environment semantics aided wireless communications: a case study of mmWave beam prediction and blockage prediction. *IEEE J Sel Areas Commun*, 41(7):2025-2040. https://doi.org/10.1109/JSAC.2023.3280966

Zeng Y, Xu XL, 2021. Toward environment-aware 6G communications via channel knowledge map. *IEEE Wirel Commun*, 28(3):84-91. https://doi.org/10.1109/MWC.001.2000327

Zeng Y, Chen JT, Xu J, et al., 2024. A tutorial on environment-aware communications via channel knowledge map for 6G. *IEEE Commun Surv Tut*, 26(3):1478-1519. https://doi.org/10.1109/COMST.2024.3364508

Zhang JH, 2016. The interdisciplinary research of big data and wireless channel: a cluster-nuclei based channel model. *China Commun*, 13(2):14-26. https://doi.org/10.1109/CC.2016.7405719

Zhang JH, Tang P, Yu L, et al., 2020. Channel measurements and models for 6G: current status and future outlook. *Front Inform Technol Electron Eng*, 21(1):39-61. https://doi.org/10.1631/FITEE.1900450

Zhang JH, Lin JX, Tang P, et al., 2023. Channel measurement, modeling, and simulation for 6G: a survey and tutorial. https://arxiv.org/abs/2305.16616

Zhang P, Zhang JH, Qi Q, et al., 2020. Ubiquitous-X: constructing the future 6G networks. *Sci Sin Inform*, 50(6):913-930 (in Chinese). https://doi.org/10.1360/SSI-2020-0068

Zhang P, Li LH, Niu K, et al., 2021. An intelligent wireless transmission toward 6G. *Intell Converg Netw*, 2(3):244-257. https://doi.org/10.23919/ICN.2021.0017

Zhang P, Xu WJ, Gao H, et al., 2022. Toward wisdom-evolutionary and primitive-concise 6G: a new paradigm of semantic communication networks. *Engineering*, 8:60-73. https://doi.org/10.1016/j.eng.2021.11.003

Zhang P, Xu XD, Dong C, et al., 2023. Model division multiple access for semantic communications. *Front Inform Technol Electron Eng*, 24(6):801-812. https://doi.org/10.1631/FITEE.2300196

Zhang Z, Zhang JH, Zhang YX, et al., 2024. Deep reinforcement learning based dynamic beam selection in dual-band communication systems. *IEEE Trans Wirel Commun*, 23(4):2591-2606. https://doi.org/10.1109/TWC.2023.3300830